



HAL
open science

Spatial and Frequency Selective Plasmonic Metasurface for Long Wavelength Infrared Spectral Region

Xiaohang Pan, Hao Xu, Yanqing Gao, Yafeng Zhang, Liaoxin Sun, Dan Li, Zhengji Wen, Shimin Li, Weiwei Yu, Zhiming Huang, et al.

► **To cite this version:**

Xiaohang Pan, Hao Xu, Yanqing Gao, Yafeng Zhang, Liaoxin Sun, et al.. Spatial and Frequency Selective Plasmonic Metasurface for Long Wavelength Infrared Spectral Region. *Advanced Optical Materials*, 2018, 6 (20), pp.1800337. 10.1002/adom.201800337 . hal-03284699

HAL Id: hal-03284699

<https://hal.science/hal-03284699>

Submitted on 30 Jul 2021

HAL is a multi-disciplinary open access archive for the deposit and dissemination of scientific research documents, whether they are published or not. The documents may come from teaching and research institutions in France or abroad, or from public or private research centers.

L'archive ouverte pluridisciplinaire **HAL**, est destinée au dépôt et à la diffusion de documents scientifiques de niveau recherche, publiés ou non, émanant des établissements d'enseignement et de recherche français ou étrangers, des laboratoires publics ou privés.

Spatial and frequency selective plasmonic metasurface for long wavelength infrared spectral region

Xiaohang Pan^{1,2}, Hao Xu², Yanqing Gao², Yafeng Zhang², Liaoxin Sun², Dan Li^{1,2},
Zhengji Wen², Shimin Li², Weiwei Yu², Zhiming Huang², Jianlu Wang², Bo Zhang², Yan Sun²,
Jinglan Sun², Xiangjian Meng², Xin Chen², Béatrice Dagens³, Jiaming Hao^{2,*}, Yue Shen^{1,†},
Ning Dai² and Junhao Chu²

¹School of Materials Science and Engineering, Shanghai University, Shanghai 200444, China

*²National Laboratory for Infrared Physics, Shanghai Institute of Technical Physics, Chinese
Academy of Sciences, Shanghai 200083, China*

*³Centre de Nanosciences et de Nanotechnologies, CNRS, Univ. Paris-Sud, Université
Paris-Saclay, C2N – Orsay, 91405, Orsay cedex, France*

*Corresponding author: jiaming.hao@mail.sitp.ac.cn

Abstract

The development of novel approaches that control absorption and emission operating in long wavelength infrared (LWIR) spectral region is of fundamental importance for many applications, such as, remote temperature sensing, environmental monitoring, thermal imaging, radiation cooling and industrial facility inspections. A high performance plasmonic metasurface-based absorber for the LWIR spectral region is presented. In our design, a pyroelectric thin film, poly(vinylidene fluoride-trifluoroethylene) (P(VDF-TrFE)) copolymer, is introduced as spacer, that offers the device not only with multiple selective high absorption bands but also promising potential for application in optoelectronics. By employing a scattering-type near-field optical microscopy (s-SNOM), both the near-field amplitude and phase optical responses of the absorber are investigated at resonant wavelength, thereby providing direct experimental evidence to verify the nature of the absorption effect. To further demonstrate the versatility of our design, a particular metasurface patterned by the building blocks of the plasmonic absorber is fabricated and characterized. Two-dimensional hyperspectral images show that such a patterned structure exhibits both frequency and spatially selective absorption.

Keyword: Perfect absorber, long wavelength infrared, plasmonic metasurface, near-field microscopy, hyperspectral infrared imaging.

1. Introduction

Long wavelength infrared (LWIR), in the commonly used division scheme of infrared detection, it corresponds to the electromagnetic radiation in the wavelength region roughly from 8 to 15 μm .^[1] Most of the thermal radiation emitted by objects on earth at room temperature falls in the spectral range, then this region is also referred to as “thermal infrared”. The development of novel approaches that control absorption and emission operating in this spectrum is fundamentally important for a variety of purposes, such as, remote temperature sensing, environmental monitoring, thermal imaging, radiation cooling, night vision and industrial facility inspections.^[2-5] Metasurfaces are man-made ultrathin photonic materials constructed by subwavelength planar units with desired electromagnetic properties, which exhibit unusual abilities to manipulate electromagnetic waves, in particular, function as high-efficiency absorbing media.^[6-10]

In this letter, we propose and experimentally demonstrate a high performance plasmonic metasurface-based absorber (PMBA) operating in the LWIR spectral region. The basic structure of our design is comprised of a layer of metallic disk array separated from an opaque plasmonic ground plate by a dielectric spacer (See **Figure 1(a)**). It notes that such metal-insulator-metal (MIM) configuration metasurfaces have been suggested as absorbers and realized at various frequencies.^[11-16] In contrast to previous designs, we incorporate a pyroelectric thin film, poly(vinylidene fluoride-trifluoroethylene) (P(VDF-TrFE)) copolymer (70/30 molar ratio),^[17,18] instead of traditional dielectric materials (such as Al_2O_3 , SiO_2 and MgF_2) for the dielectric

spacer. This change not only brings our design with high performance multiple selective absorption bands resulting from the unique optical properties of the copolymer, but also makes it has great prospects for applications in compact optoelectronic devices such as uncooled LWIR pyroelectric detectors.^[19-21]

We note that perfect absorption in metasurface-based absorbers originated from localized electromagnetic resonances in the structures, the physical origin of the high absorption effect, has been pointed out. To illuminate the mechanism, electromagnetic field distributions at the working wavelengths obtained by numerical simulations have also been widely investigated so far. But there is little work to experimentally verify this argument. Here we map the spatial near-field distributions of our proposed absorber around resonance using phase-resolved scattering-type near-field optical microscopy (s-SNOM) and compare the experimental results with numerical simulations.^[22, 23] Finally, to further elucidate the functionality of our absorber design, we pattern a structure based on the PMBA, which exhibits both frequency and spatially selective absorption and investigate its corresponding hyperspectral thermal infrared imaging.

2. Results and Discussion

Because of the lack of the accurate optical constants of P(VDF-TrFE) copolymer, we firstly perform experiments to determine the optical properties of the copolymer by using infrared variable-angle spectroscopic ellipsometry (IR-VASE). Figures 1(c) and 1(d) respectively show the measured ellipsometry data Ψ and Δ (dashed-dotted curves) for a 200-nm-thick P(VDF-TrFE) copolymer thin film in the spectral range

600– 6000 cm^{-1} (16.7–1.6 μm) at incident angles $\theta = 60^\circ, 70^\circ$. For definition of the ellipsometric parameters Ψ and Δ and detail information of spectroscopic ellipsometry, please refer to the ref. 24. The complex refractive index components n and k are then extracted by model fitting the experimental spectroscopic ellipsometric data (see Figures 1(c) and 1(d), solid curves), and presented Figures 1(e) and 1(f), respectively. It is observed that the pyroelectric copolymer possesses a set of strong molecular vibrational modes in the LWIR spectral range.^[25-27]

We now perform numerical simulations to investigate the absorbance (A) of the designed absorber with different values of the critical geometric parameters. The simulations are conducted using commercial package Lumerical FDTD solutions based on finite-difference-time-domain (FDTD) method. Owing to the presence of the continuous metallic ground plate (aluminum with the thickness $h = 100$ nm), the transmittance (T) of the device is nearly zero over the entire wavelength range we concerned. The absorbance (A) can thus be obtained using a simple formula $A=1-R$, where R denotes the reflectance, which can be directly obtained by numerical simulations. In the main text, we only concentrate on how the absorbance of the proposed device varies against the thickness (l) of spacer layers, the relationship between the absorption properties and the periodicity (p), the diameter (d) and the thickness (t) of metallic disks are presented in the supporting information as shown in Figures S1, S2 and S3, respectively.^[28] **Figure 2(a)** shows the simulated absorbance spectra for four different thickness spacer layers ($l = 0.3, 0.37, 0.45, \text{ and } 0.52\mu\text{m}$) at normal incidence, with other parameters $d = 3 \mu\text{m}$, $t = 50$ nm, and $p = 6 \mu\text{m}$. As

shown in Figure 2(a), when thickness $l = 0.37\mu\text{m}$ (denoted by “PMBA-S1” hereinafter), the absorbance can be as high as 99.5% at the wavenumber of 980 cm^{-1} ($10.2\mu\text{m}$). For $l = 0.52\mu\text{m}$ case, at the wavenumber of 825 cm^{-1} ($12.1\mu\text{m}$), the maximum absorbance reaches over 99% as well.

In order to experimentally demonstrate this effect, the absorbers are fabricated on a polished silicon wafer with standard microfabrication techniques. Figure 1(b) displays a scanning electron microscopy (SEM) image of a fabricated sample which adopts the optimized geometric parameters of PMBA-S1. Transmission and reflection of these devices are characterized using a Fourier transform infrared (FTIR) spectrometer (Bruker IFS 125HR). The transmission is measured at the normal incidence and reflection is measured at incident angle of 15° . Figure 2(b) shows the spectra of experimental absorbance, which are obtained based on the measured transmittance and reflectance. Reasonable agreements are found when compare the experimental spectra with the numerical simulated. For thickness $l = 0.37$ (0.52) μm , the maximum absorption is close to 95.5% (97%) at the wavenumber of 981 (829) cm^{-1} in experiment. In addition, from both the numerical simulated and experimental results, one can see that for each case, the absorber exhibits three distinct absorption peaks. More notably, it is found that all of these high performance absorption peaks are attributed to the excitation of the fundamental cavity resonant mode (The evidence is presented in the supporting information as shown in Figure S4). This is in sharp contrast to the multispectral metamaterial absorbers reported in the literatures, in which the multiband high performance absorption is due to either the hybrid

multi-resonant unit structures or simultaneously exciting several high-order localized electromagnetic resonant modes.^[29-32]

We further reveal that such multiband absorption effect is strongly related to the unique optical constants of the P(VDF-TrFE) copolymer spacer. To figure out the physical phenomenon, time-averaged dissipative power (TADP) is theoretically investigated. For example, Figure 2(c) shows the normalized TADPs (P_{loss} / P_{in}) spectra for the total and each component of the PMBA-S1. As can be observed, for the two absorption peaks of 825 cm^{-1} ($12.1 \text{ }\mu\text{m}$) and 869 cm^{-1} ($11.5 \text{ }\mu\text{m}$), more than 78% and 87% energy of incident radiation are dissipated by the copolymer spacer, respectively, while for the absorption peak of 980 cm^{-1} , energy dissipation by the spacer is less than 58%. This is exactly thanks to the optical properties of the copolymer spacer, which exhibit two strong infrared-active vibrational modes around the two long-wavelength absorption peaks and have rather larger attenuation factors compared to that of the short-wavelength absorption peak (see Figure 1(e)).

To visualize and better understand the nature of our absorber device, we utilize s-SNOM (Neaspec) to investigate the near-field response of our fabricated absorber, which can provide near-field optical signal amplitude and phase by interferometric detection of scattered light with a phase-modulated reference wave. **Figures 3(a)** and **3(b)** show the experimental near-field amplitude and phase images of vertical electric field component E_z for the $l = 0.37 \text{ }\mu\text{m}$ structure recorded at $\lambda = 10.2 \text{ }\mu\text{m}$. As one can see, the amplitude shows noticeable enhancement on the surface of metallic disks, the phase signal has a remarkable variation of about 180° at the disk center. The images

provide direct experimental evidence that such high performance absorption effect is as expected owing to the fundamental dipolar-like near-field resonant mode. Numerical simulations are also conducted for this structure. The corresponding amplitude and phase near-field images are displayed in Figures 3(c) and 3(d). Good agreements are noted between the numerical and experimental results.

In order to investigate the angular response of optical performance of the PMBAs, additional optical measurements and numerical simulations are performed. **Figures 4(a) and 4(b)** display the measured reflectance of the sample shown in Figure 1(b) as a function of wavenumber and the in-plane wave vector $k_x = k_0 \sin \theta$ for both TE and TM polarizations, respectively. The corresponding simulated reflectance spectra for the both polarizations are presented in Figures 4(c) and 4(d), which are in good agreement with the experimental data. Our experimental and numerical results show that for TM polarization, a clear anticrossing behavior is observed for the absorption peak 980 cm^{-1} at the incident angle of $\theta = 45^\circ$. The reason for this angular characteristic is that the oblique incident wave is diffracted by the first-order reciprocal vectors of the periodic disk array, and exciting the surface plasmon polariton (SPP) supported by the air-spacer-metal multilayer, which thus strongly couples with and disturbs the localized resonant mode.^[33-35] Nevertheless, for the TE polarization, the anticrossing point is absent. This is due to that although the diffracted wave is also introduced for high incident angles, which is no longer interfering with the localized resonant mode, since the multilayer cannot support TE surface modes.^[36] It is worth mentioning that diffraction beams are introduced by the periodic structures

for both polarizations and play the roles of new channels for wave scattering at high incident angles. As a result, the absorption performances would be highly decreased. This opens a window for our design to function as optical devices with directional and frequency-selective absorption/emission properties.^[35]

For further demonstration of the versatility of the PMBA and its prospect in practical applications, we experimentally pattern a metasurface, which exhibits both frequency and spatially selective absorption properties.^[37] **Figure 5(a)** shows an optical microscope image of the patterned metasurface, printing the two letters “IR” (the abbreviation of Infrared). In this design, the basic building block of the plasmonic absorber PMBA-S1 is used to form the pattern of the letters. The pattern contains a total of more than 22000 plasmonic unit cells. The minimum feature size of the letters is about 150 μm . The unit cell of background area has the identical lateral dimensions as S1, i.e., 6 μm \times 6 μm , and consists of the same metallic ground plate and P(VDF-TrFE) copolymer with identical thicknesses, but no metallic disk on the top. We characterize the sample using a FTIR combined with an infrared microscope. The sample stage can be moved automatically and is controlled by a computer. A spatial resolution of 50 μm is adopted, thus generating an image with 40 pixels along both x and y axes. For each pixel, the reflection spectrum is collected in the ranges 600 - 6000 cm^{-1} with the spectral resolution of 2 cm^{-1} . Eventually, two-dimensional hyperspectral images are obtained, with a total data record size of 4.3×10^6 . These allow us to fully study the absorption property of the sample.

The experimental absorbance spectrum of the background is shown in Figure 5(b)

as the dashed blue curve (denoted by Area 1), which is recorded at the position labeled by the blue spot in Figure 5(a) and exhibits low absorption performance over the LWIR spectral range. For comparison, in Figure 5(b) we also plot the absorbance spectra of the area composed of PMBA-S1 (solid red curve, Area 2) recorded at the position labeled by the red spot in Figure 5(a). As expected, the absorption of this area is identical to the one presented in Figure 2(b) as the solid red curve. The 2D and 3D images of the experimental absorbance data for the absorption peak wavelength of $10.2\ \mu\text{m}$ ($980\ \text{cm}^{-1}$) are displayed in Figures 5(c) and 5(d), respectively. As can be observed from these two images, at this resonant wavelength, the pattern composed of the PMBA achieves nearly ideal absorption. To illustrate the frequency dependence of the spatially selective structure, Figures 5(e) and 5(f) respectively show 2D and 3D images for a wavelength of $14\ \mu\text{m}$ ($714\ \text{cm}^{-1}$). We can see that in contrast to the optical photograph (Figure 5(a)) and the images at $10.2\ \mu\text{m}$ (Figures 5(c) and 5(d)), at $14\ \mu\text{m}$ the pattern cannot be so clearly distinguished from the background.

3. Conclusion

In summary, we have presented a plasmonic metasurface-based ideal absorber for the LWIR spectral range. In our design, a pyroelectric thin film, P(VDF-TrFE) copolymer, is introduced as the spacer layer, which not only brings our device with multiple selective high absorption bands, but also offers a further step towards the development of the compact optoelectronic devices. The angle resolved optical responses show that the absorber is sensitive to the incident angles and can be controlled by the periodicity of the disk array. This opens another window for our

design to function as optical devices with directional and frequency-selective absorption/emission characteristics. To better understand the origin of the absorption effect, we applied interferometric near-field microscopy to map both the near-field amplitude and phase optical responses of the absorber, and the obtained images provide direct experimental evidence to confirm that such high performance absorption effect is exactly due to the excitation of the fundamental electromagnetic resonant mode. We further patterned a metasurface based on the PMBA, which exhibits both frequency and spatially selective absorption. The above listed advances suggest that the absorber has various promising potential applications, including thermal infrared light sources, thermal management, and hyperspectral thermal imaging.

4. Experimental section:

IR-VASE characterizations. A 200-nm-thick P(VDF-TrFE) copolymer (70/30 molar ratio) thin films are prepared on electronic-grade Si(100) wafer by spin-coating method for ellipsometric measurements. Spectroscopic ellipsometry measurements are performed using an infrared variable angle spectroscopic ellipsometry system (IR-VASE, J. A. Woollam). Lorentz model with multiple oscillators is used to fit the experimental data.

Numerical simulations. Full field electromagnetic wave simulations are conducted using commercial package Lumerical FDTD solutions based on finite-difference-time-domain method. In our simulations, both the optical constants

of gold and aluminum are taken from Ref. 38. Reflection and Transmission are respectively collected with power monitors behind the incident plane wave and the structure. Electromagnetic field distributions are recorded by 2D field profile monitors at the corresponding observation positions presented in the text.

Sample fabrication: The LWIR absorber samples are fabricated using the techniques of direct laser lithography and wet-chemical lift-off. Clean silicon substrates are coated with the bottom Al layer and P(VDF-TrFE) copolymer spacer by magnetron sputtering and spin-coating methods, respectively. And then, the disk array is defined by in AZ5214 photoresist using direct laser lithography. A 50-nm-thick gold is then deposited using magnetron sputtering. Complete devices are achieved by removing the photoresist mark in alcohol solutions.

Optical measurements. The angle resolved reflection spectra measurements are performed by using a Fourier transform infrared spectrometer (Bruker IFS 125HR), which is equipped with reflection module allowing for angles ranging for 15° to 80° . The measured reflection spectra are normalized with respect to a gold mirror. A wire-grid infrared polarizer is placed in the light path to obtain both TE and TM polarization spectra. Two-dimensional hyperspectral images of the pattern sample are characterized with the Thermo Fisher microscopic Fourier infrared spectrometer.

Near field microscopy. The near-field optical response amplitude and phase of the

absorber devices are characterized by employing a commercial s-SNOM (Neaspec GmbH, Germany). Our near field microscopy is equipped with a tunable quantum cascade laser with operating wavelengths range of 7.8 - 10.5 μm . Nano-scale-resolved images can be obtained by collecting of the infrared light scattered at an atomic force microscope tip with a phase-modulated reference wave.

Acknowledgements

This work is supported by National Key R&D Program of China (2017YFA0205801), National Natural Science Foundation of China (61471345), the National Young 1000 Talent Plan, GDRI Sino-French Optoelectronics and Photonics – Photonet, and Shanghai Science and Technology Committee (16JC1403500).

References

- [1] J. Byrnes, *Unexploded Ordnance Detection and Mitigation*, Springer, NY, USA **2008**.
- [2] S. P. Mahulikar, H. R. Sonawane, G. Arvind Rao, *Progress in Aerospace Sciences*. **2007**, *43*, 218.
- [3] P. Colarusso, L. H. Kidder, I. W. Levin, J. C. Fraser, J. F. Arens, E. Neillewis, *Appl. Spectrosc.* **1998**, *52*, 106.
- [4] R. Bhargava, *Appl. Spectrosc.* **2012**, *66*, 1091.
- [5] Y. Zhai, Y. Ma, S. N. David, D. Zhao, R. Lou, G. Tan, R. Yang, X. Yin, *Science*. **2017**, *355*, 1062.
- [6] N. Yu, F. Capasso, *Nat. Mater.* **2014**, *13*, 139.
- [7] T. D. Dao, K. Chen, S. Ishii, A. Ohi, T. Nabatame, M. Kitajima, T. Nagao, *Acs Photonics*, **2015**, *2*, 964.
- [8] W. Wang, Y. Qu, K. Du, S. Bai, J. Tian, M. Pan, H. Ye, M. Qiu, Q. Li, *Appl. Phys. Lett.* **2017**, *110*, 101101.
- [9] J.W. Stewart, G. M. Akselrod, D. R. Smith, M. H. Mikkelsen, *Adv. Mater.* **2017**, *29*, 1602971.
- [10] W. Li, J. Valentine, *Nano letters*, **2014**, *14*, 3510.
- [11] A. Tittl, A. U. Michel, M. Schäferling, X. Yin, B. Gholipour, L. Cui, M. Wuttig, T. Taubner, F. Neubrech, H. Giessen, *Adv. Mater.* **2015**, *27*, 4597.
- [12] J. Hao, L. Zhou, M. Qiu, *Phys. Rev. B.* **2011**, *83*, 165107.
- [13] K. Lee, S. Seo, L. Jay Guo, *Adv. Opt. Mater.* **2015**, *3*, 347.

- [14] J. Hao, J. Wang, X. Liu, W. J. Padilla, L. Zhou, M. Qiu, *Appl. Phys. Lett.* **2010**, *96*, 251104.
- [15] N. Liu, M. Mesch, T. Weiss, M. Hentschel, H. Giessen, *Nano Lett.* **2010**, *10*, 2342.
- [16] H. Tao, C. M. Bingham, A. C. Strikwerda, D. Pilon, D. Shrekenhamer, N. I. Landy, K. Fan, X. Zhang, W. J. Padilla, R. D. Averitt, *Phys. Rev. B*, **2008**, *78*, 241103.
- [17] A.V. Bune, V. M. Fridkin, S. Ducharme, L. M. Blinov, S. P. Palto, A.V. Sorokin, S. G. Yudin, A. Zlatkin, *Nature*. **1998**, *391*, 874.
- [18] B. Neese, B. Chu, S. Lu, Y. Wang, E. Furman, Q. M. Zhang, *science*, **2008**, *321*, 821.
- [19] J.Y. Suen, K. Fan, J. Montoya, C. Bingham, V. Stenger, S. Sriram, W.J. Padilla, *Optica*, **2017**, *4*, 276.
- [20] J. Song, H. Lu, A. Gruverman, S. Ducharme, *Appl. Phys. Lett.* **2014**, *104*, 192901.
- [21] T. D. Dao, S. Ishii, T. Yokoyama, T. Sawada, R. P. Sugavaneshwar, K. Chen, Y. Wada, T. Nabatame, Tadaaki Nagao, *ACS Photonic*, **2016**, *3*, 1271.
- [22] P. A. Gonzalez, M. Schnell, P. Sarriugarte, H. Sobhani, C. Wu, N. Arju, A. Khanikaev, F. Golmar, P. Albella, L. Arzubiaga, F. Casanova, L. E. Hueso, P. Nordlander, G. Shvets, R. Hillenbrand, *Nano Lett.* **2011**, *11*, 3922.
- [23] T. G. Habteyes, *J. Phys. Chem. C*, **2014**, *118*, 9119.
- [24] H. Fujiwara, *Spectroscopic Ellipsometry: Principles and Applications* Wiley,

Ibaraki, Japan **2007**.

- [25] M. Bai, M. Poulsen, A. V. Sorokin, S. Ducharme, C. M. Herzinger, V. M. Fridkin, *J. Appl. Phys.* **2003**, *94*, 195.
- [26] M. Bai, A. V. Sorokin, D. W. Thompson, M. Poulsen, S. Ducharme, C. M. Herzinger, S. Palto, V. M. Fridkin, S. G. Yudin, V. E. Savchenko, L. K. Gribova, *J. Appl. Phys.* **2004**, *95*, 3372.
- [27] J. L. Wang, Y. Q. Gao, Z. M. Huang, X. J. Meng, S. Z. Yuan, J. Yang, J. L. Sun, J. H. Chu, *Ferro*, **2010**, *405*, 120.
- [28] C. Qu, S. Ma, J. Hao, M. Qiu, X. Li, S. Xiao, Z. Miao, N. Dai, Q. He, S. Sun, L. Zhou, *Phys. Rev. Lett.* **2015**, *115*, 235503.
- [29] Y. Cui, Y. He, Y. Jin, F. Ding, L. Yang, Y. Ye, S. Zhong, Y. Lin, S. He, *Laser & Photonics Rev.* **2014**, *8*, 495.
- [30] I. J. H. McCrindle, J. Grant, T. D. Drysdale, D. R. S. Cumming, *Adv. Opt. Mater.* **2014**, *2*, 149.
- [31] Y. Peng, X. Zang, Y. Zhu, C. Shi, L. Chen, B. Cai, S. Zhuang, *Opt. Express.* **2015**, *23*, 2032.
- [32] K. Aydin, V. E. Ferry, R. M. Briggs, H. A. Atwater, *Nat. Commun.* **2011**, *2*, 517
- [33] B. I. Afinogenov, D. S. Kopylova, K. A. Abrashitova, V. O. Bessonov, A. S. Anisimov, S. A. Dyakov, N. A. Gippius, Y. G. Gladush, A. A. Fedyanin, A. G. Nasibulin, *Phys. Rev. Applied.* **2018**, *9*, 024027.
- [34] P. Jouy, Y. Todorov, A. Vasanelli, R. Colombelli, I. Sagnes, C. Sirtori, *Appl.*

Phys. Lett. **2011**, *98*, 021105.

- [35] D. Costantini, A. Lefebvre, A.-L. Coutrot, I. Moldovan-Doyen, J.-P. Hugonin, S. Boutami, F. Marquier, H. Benisty, J.-J. Greffet, *Phys. Rev. Applied.* **2015**, *4*, 014023.
- [36] S. A. Maier, *Plasmonics: Fundamentals and Applications*, Springer, NY, USA, **2007**.
- [37] X. Liu, T. Starr, A. F. Starr, W. J. Padilla, *Phys. Rev. Lett.* **2010**, *104*, 207403.
- [38] M. J. Webber, *Handbook of Optical Materials*, CRC, BR, USA **2003**.

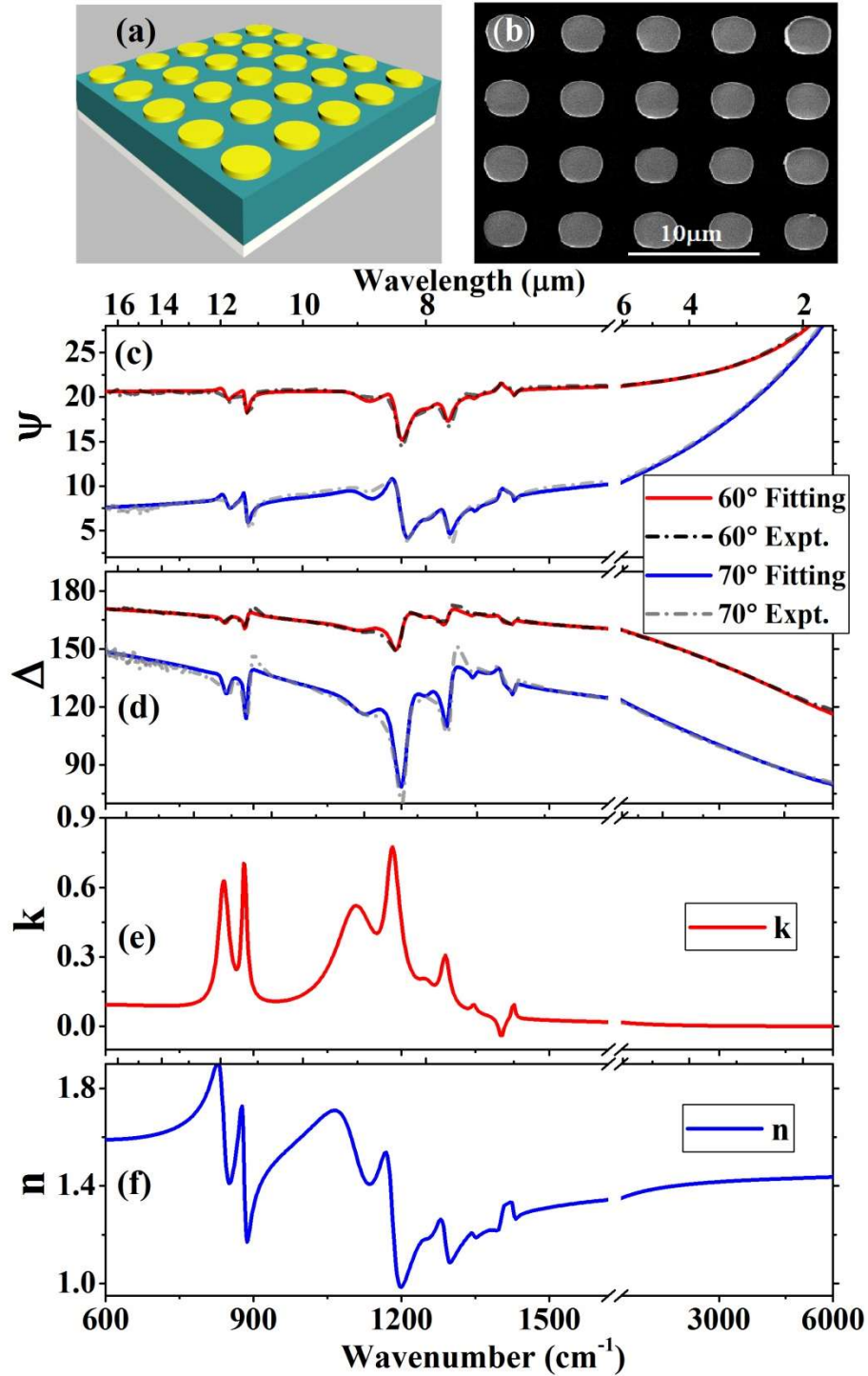


Figure 1. (a) Schematics of the LWIR metasurface-based absorber. (b) SEM image of an experimental sample. (c) and (d) IR-VASE data of Ψ and Δ (dashed-dotted curves) for a 200-nm-thick P(VDF-TrFE) copolymer thin film at angles of incidence $\theta = 60^\circ$ and 70° , and the fitted results from the multiple oscillators Lorentz model (solid curves). (e) Real and (f) imaginary parts of refractive index for the P(VDF-TrFE) copolymer obtained from the Ellipsometry data analysis.

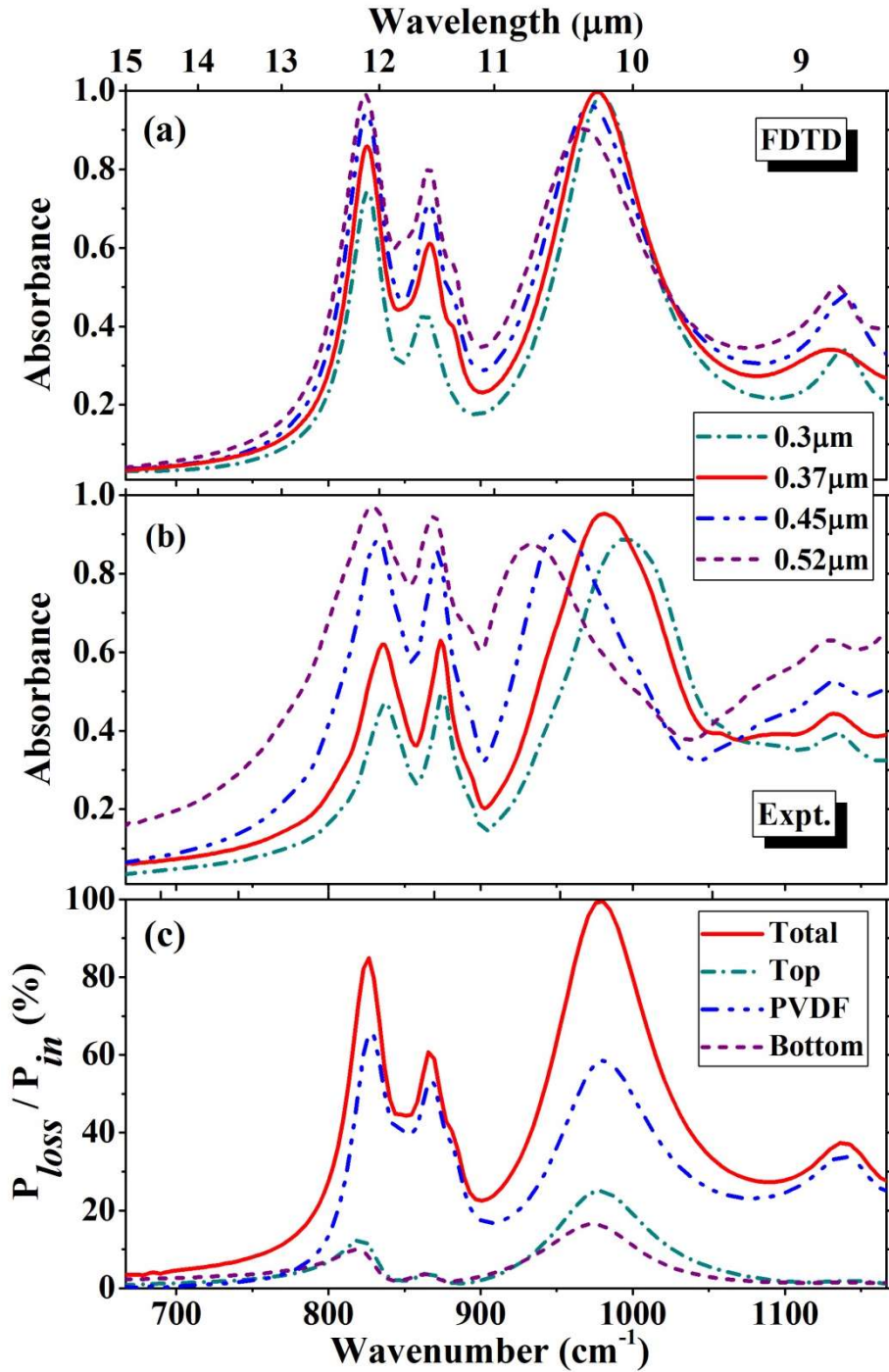


Figure 2. (a) Simulated and (b) measured absorbance spectra for the samples with four different thickness P(VDF-TrFE) copolymer spacers. (c) The normalized time-averaged dissipative power spectra for the total and each component (top Au disk, P(VDF-TrFE) copolymer spacer, and bottom Al mirror) of the $l = 0.37 \mu\text{m}$ absorber device.

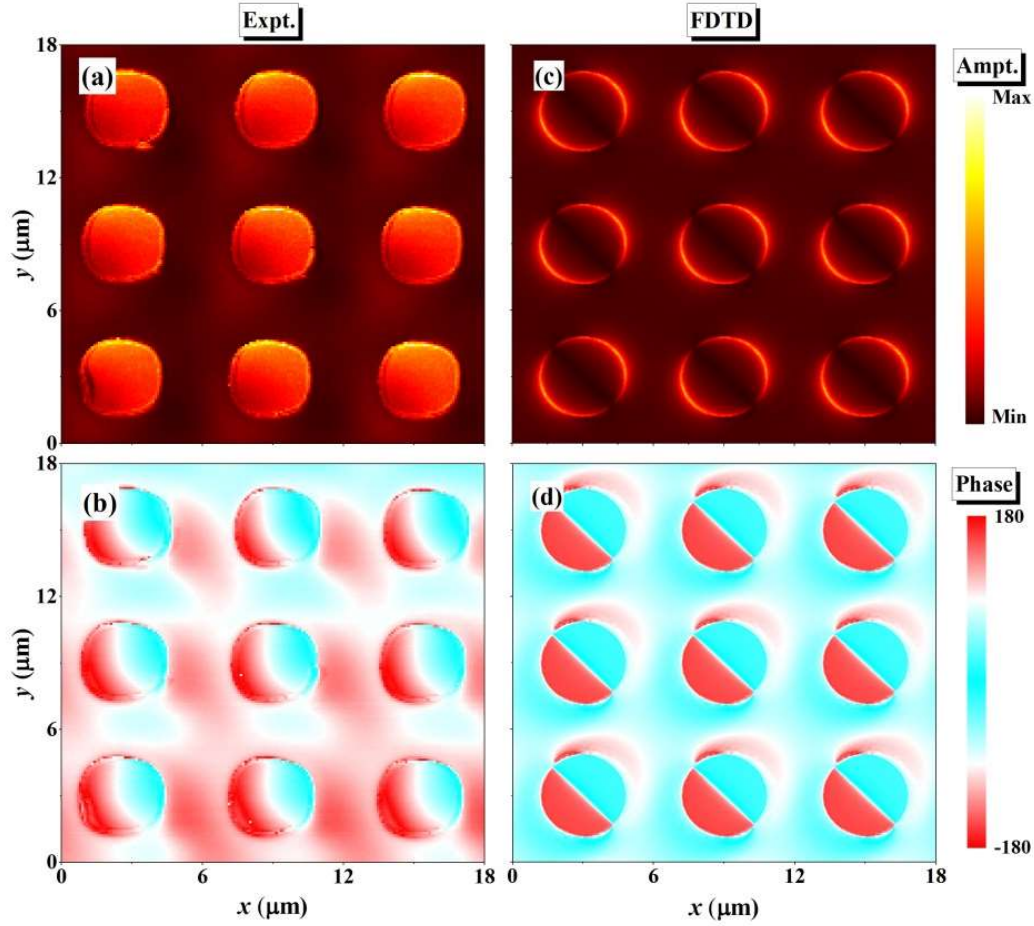


Figure 3. (a) and (b) Experimental near-field amplitude and phase images of the vertical electric component for the $l = 0.37 \mu\text{m}$ absorber device mapped at the wavelength of $10.2 \mu\text{m}$. (c) and (d) Simulated near-field amplitude and phase images of the corresponding model system.

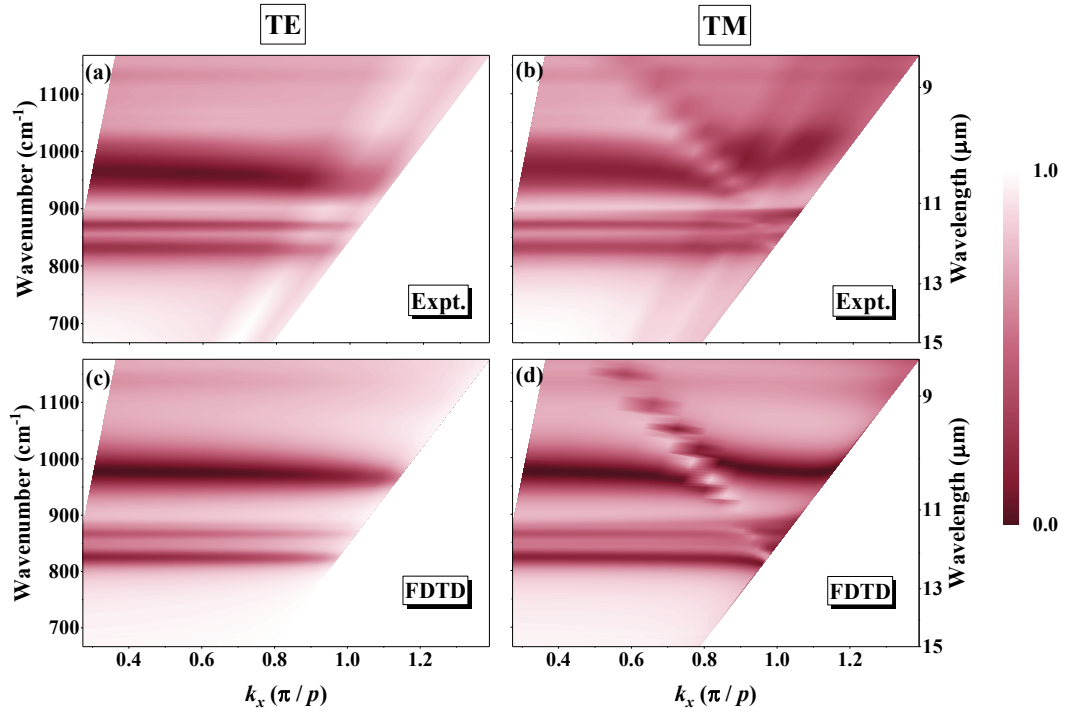


Figure 4. (a) and (b) Measured reflectance of the $l = 0.37 \mu\text{m}$ absorber device as a function of wavenumber and in plane wave vector k_x for both TE and TM polarizations. (c) and (d) The corresponding simulated reflectance spectra for both TE and TM polarizations.

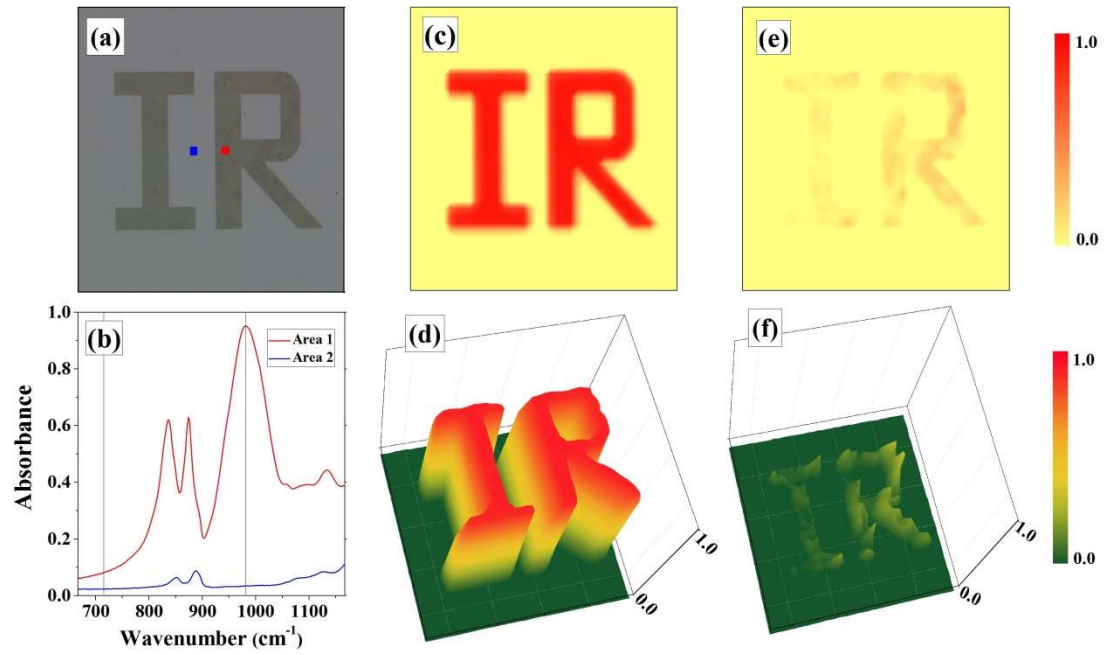


Figure 5. (a) An optical microscope image of the patterned spatially dispersive metasurface. (b) The experimental absorbance of the background and the area composed of the metasurface-based absorber. (c) 2D and (d) 3D images of the experimental absorption at 10.2 μm . (e) 2D and (f) 3 images of absorption at 14 μm .